ANL/NSE-19/15

Initial Industry Collaborations of the Center of Excellence

Nuclear Science and Engineering Division

About Argonne National Laboratory
Argonne is a U.S. Department of Energy laboratory managed by UChicago Argonne, LLC under contract DE-AC02-06CH11357. The Laboratory's main facility is outside Chicago, at 9700 South Cass Avenue, Argonne, Illinois 60439. For information about Argonne and its pioneering science and technology programs, see www.anl.gov.

DOCUMENT AVAILABILITY

Online Access: U.S. Department of Energy (DOE) reports produced after 1991 and a growing number of pre-1991 documents are available free at OSTI.GOV (http://www.osti.gov/), a service of the US Dept. of Energy's Office of Scientific and Technical Information.

Reports not in digital format may be purchased by the public from the National Technical Information Service (NTIS):
U.S. Department of Commerce
National Technical Information Service
5301 Shawnee Rd
Alexandria, VA 22312
www.ntis.gov
Phone: (800) 553-NTIS (6847) or (703) 605-6000
Fax: (703) 605-6900
Email: **orders@ntis.gov**

Reports not in digital format are available to DOE and DOE contractors from the Office of Scientific and Technical Information (OSTI):
U.S. Department of Energy
Office of Scientific and Technical Information
P.O. Box 62
Oak Ridge, TN 37831-0062
www.osti.gov
Phone: (865) 576-8401
Fax: (865) 576-5728
Email: **reports@osti.gov**

Disclaimer
This report was prepared as an account of work sponsored by an agency of the United States Government. Neither the United States Government nor any agency thereof, nor UChicago Argonne, LLC, nor any of their employees or officers, makes any warranty, express or implied, or assumes any legal liability or responsibility for the accuracy, completeness, or usefulness of any information, apparatus, product, or process disclosed, or represents that its use would not infringe privately owned rights. Reference herein to any specific commercial product, process, or service by trade name, trademark, manufacturer, or otherwise, does not necessarily constitute or imply its endorsement, recommendation, or favoring by the United States Government or any agency thereof. The views and opinions of document authors expressed herein do not necessarily state or reflect those of the United States Government or any agency thereof, Argonne National Laboratory, or UChicago Argonne, LLC.

ANL/NSE-19/15

Initial Industry Collaborations of the Center of Excellence

prepared by
Dillon Shaver, Rui Hu, Prasad Vegendla, Ling Zou, and Elia Merzari
Nuclear Science and Engineering Division, Argonne National Laboratory

June 30th, 2019

(Page intentionally left blank)

SUMMARY

The NEAMS program aims to develop an integrated multi-physics simulation capability “pellet-to-plant” for the design and analysis of future generations of nuclear power plants. In particular, the Reactor Product Line code suite's multi-resolution hierarchy is being designed to ultimately span the full range of length and time scales present in relevant reactor design and safety analyses, as well as scale from desktop to petaflop computing platforms. In particular the NEAMS program is supporting the development of novel thermal-hydraulic codes.

The Center of Excellence for Thermal Fluids Application in Nuclear Energy, launched in 2018, has as its key goals to serve as a front door to industry. The Center of Excellence for Thermal Fluids Applications in Nuclear Energy has recently launched a program to start collaborative efforts between the laboratories and industry with the objective of stimulating cooperation and increasing adoption of T/H tools developed under NEAMS by the industry-at-large.

In particular, two industry partners agreed to participate in pilot short-term collaborations aimed at demonstrating the value of NEAMS tools to their designs. These are BWXT and Kairos who proposed projects related to HTGR and FHR designs respectively. In this report we present the results of these collaborations.

1. Introduction

The Center of Excellence for Thermal Fluids Applications in Nuclear Energy has recently launched a program to start collaborative efforts between the laboratories and industry with the objective of stimulating cooperation and increasing adoption of T/H tools developed under NEAMS by the industry-at-large.

In December 2019 the center held a meeting focused on collaboration with industry. The collaboration program was launched at the meeting. Moreover, two industry partners agreed to participate in pilot short-term collaborations aimed at demonstrating the value of NEAMS tools to their designs. These are BWXT and Kairos Power who proposed projects related to HTGR and FHR designs respectively.

The diagram below aims to illustrate the role of these short-term projects. The feedback from industry has been overwhelmingly positive. We note that these short term projects are not aimed at providing a funding venue and they are not aimed at providing a mean to address problems that require protection of IP. That need is served by Gateway for Advanced Innovation in Nuclear (GAIN) vouchers. Rather, these short term projects are aimed at fulfilling the role of the center as a "front-door" to industry. They can be used by industry to propose short term activities aimed at demonstrating the tools in preparation for larger proposals. The potential paths of industrial customers are illustrated in the diagram below reflecting different levels of commitment from the industry partner.

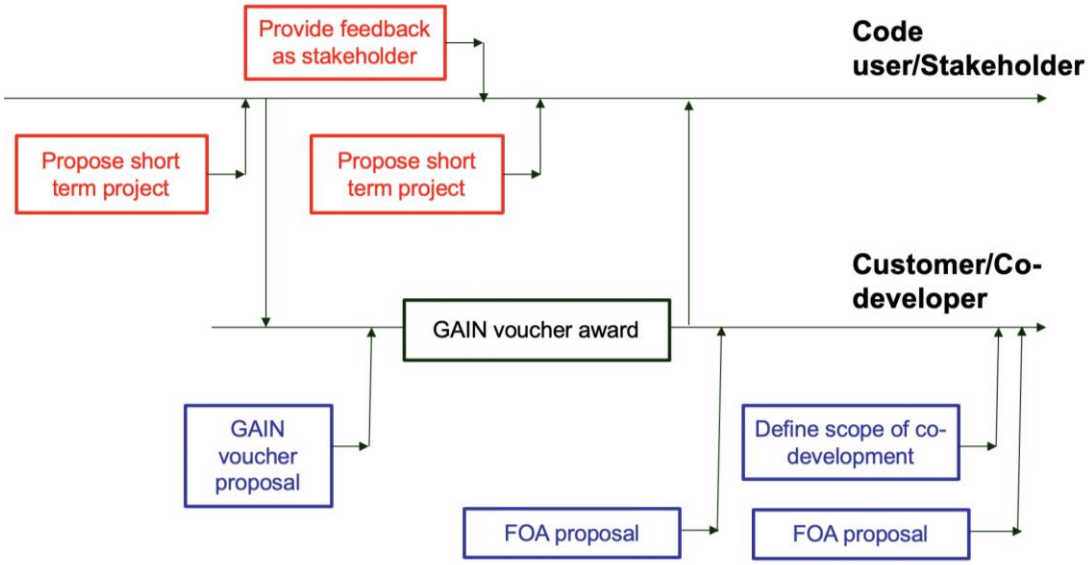

Diagram 1. Potential paths for industry collaboration in the center.

Once short term projects are completed, industry partners can propose additional work under the GAIN program working with our lab team members. This can also lead to additional funding opportunities through a funding opportunity announcement (FOA) proposal and eventually lead to co-development of codes or projects. Alternatively, the industry partner can choose to remain less involved, through repeated short-term proposals and as a stake-holder.

In the following sections the results of the first two pilot projects with Kairos and BWXT are presented.

2. BWXT Project

Under the support of DOE-NE's Nuclear Energy Advanced Modeling and Simulation (NEAMS) - Center of Excellence for Thermal Fluids Applications in Nuclear Energy, an effort had been pursued to support High Temperature Gas Reactors (HTGR) modeling and simulation needs, as part of industry engagement efforts. As integral-effects standard problems are foundational to the methodologies employed by the industry user community to verify the adequacy of computer codes and evaluation models, this effort focus on developing a standard HTGR problem for whole-system transient evaluations.

In this work, the Modular High Temperature Gas Reactor (MHTGR) was selected as a reference design for the primary loop simulations using the System Analysis Module (SAM) [1] code under both normal and accident operating conditions. SAM is under development at Argonne National Laboratory to provide fast-running, improved-fidelity, whole-plant transient analyses for advanced non-LWRs. The initial development focus was on SFRs, but more recently, SAM has been expanded to support liquid-salt-cooled and gas-cooled reactor technologies. SAM leverages modern advanced software environments and numerical methods and is well suited to be further developed as a key tool for HTGR modeling & simulation at the reactor plant scale and for reactor safety analysis.

2.1 SAM MHTGR Model

The reactor geometry and active core layout are shown in Figures 1 and 2. The active core consists of three fuel rings, the inner ring, composed of 30 fuel assemblies, the middle ring, composed of 36 assemblies, and the outer ring, also composed of 36 assemblies [2]. Each fuel assembly consists of multiple coolant channels and heat structures such as fuel, graphite and cladding. The geometry details and operating conditions are provided in Tables 1 and 2.

The block-channel model uses a unit-cell approximation which only represents the fuel assembly which includes a coolant channel, fuel, graphite and cladding. It is not suitable for reactor transients (such as PCC events) that rely heavily on core radial heat conduction for heat removal.

In the simplified ring model, each ring of fuel assemblies is represented by 1 average coolant channel and 2 average heat structures. The coolant channel was located between two heat structure rings. The heat structure ring thickness was calculated based on the material volume to represent actual geometry dimensions. Hence, the active core (fuel assemblies) was simulated with 9 circular rings where 6 rings were used for the homogenized fuel heat structure and 3 rings for the gas coolant. Apart form the fuel assemblies, six more rings were included to represent the inner reflector, outer reflector, core barrel, RPV, RPV coolant channel, and reactive cavity cooling system (RCCS).

The detailed ring ring approach was based on a specified coolant channel pitch of fuel assembly. In this detailed ring model, each fuel assembly represents 11 coolant channels and 22 heat structures. Each coolant channel was located between two heat structure rings. The heat structure ring thickness was calculated based on the material volume to represent actual geometry dimensions. Hence, the active core (fuel assemblies) was simulated with 99 circular rings where 66 rings were used for the homogenized fuel heat structure and 33 rings for the gas coolant.

The simplified ring model was similar to the detailed ring model except fuel assemblies were represented with fewer coolant channels and homogenized fuel heat structures. We had shown only results for the detailed ring model due to its detailed representation of the MHTGR and its suitability to simulate both normal and accident scenarios. In simplified ring model, the solid temperature in the fuel rings was over-predicted mainly due to the unrealistic thickness of the fuel pins.

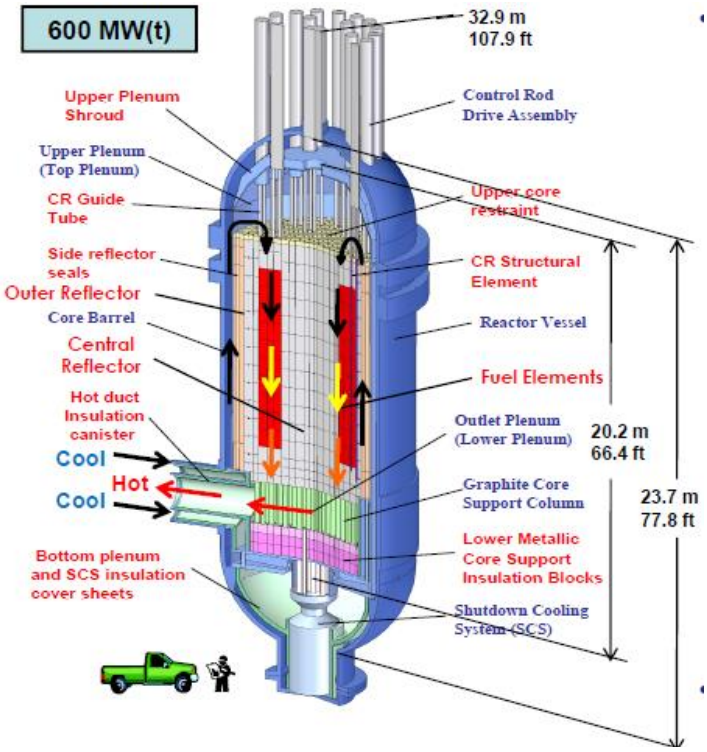

Figure 1. 600 MW MHTGR design [2]

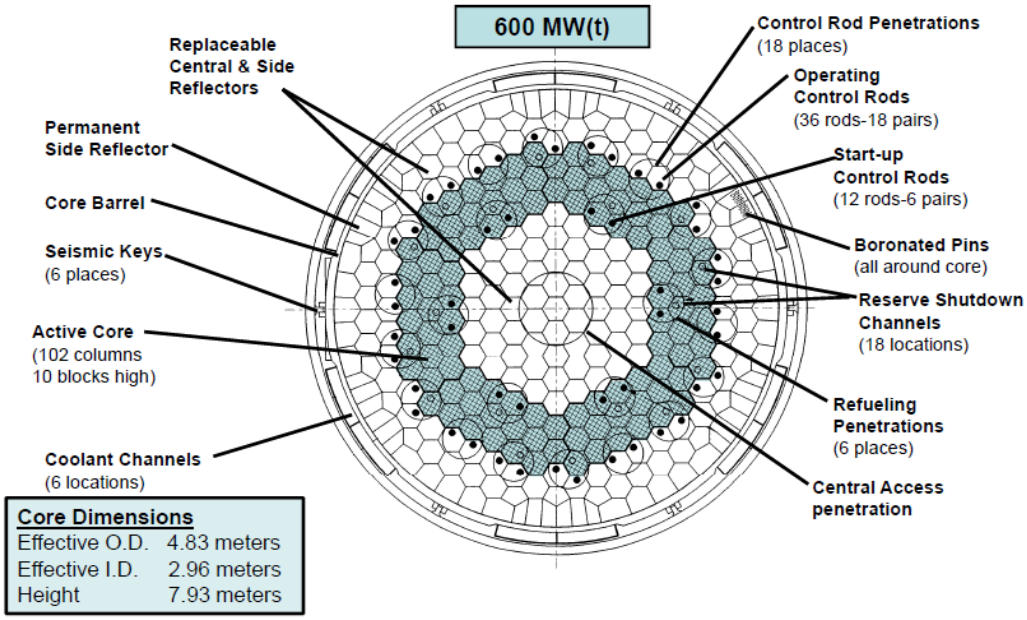

Figure 2. Active core layout [2]

Table 1. Fluid properties and operating conditions

Pressure [MPa]	7.0
Viscosity [Pa-s]	3.31E-05
Inlet core temperature [K]	623.15
Outlet core temperature	1023.15
Specific heat @ inlet [J/kg-K]	5188
Conductivity @ inlet [W/m-K]	0.2619
Density @ inlet [kg/m^3]	5.36
Mass flow rate in core [kg/s]	289.13
Mass flow rate per channel [kg/s]	0.0278
Velocity [m/s]	26.19
Reynolds number	1.38E+05
Power [MW]	600

Table 2. Core design parameters

Fuel compact per fuel hole	0.933
Fuel holes	210
No. of rods	3126
No. of fuel particles [Millions]	17.2
Graphite [kg]	90
Fuel assembly [kg]	122
Control channel [inch]	4
No. of coolant channels	102
Coolant channel dia. [mm]	15.875
Triangular pitch between coolant channels [mm]	32.6
Edges [mm]	208
Width [mm]	416
Depth [mm]	360
No. of fuel assemblies	102

Several models were developed in SAM to simulate the reactor core. The three approaches used were: (i) unit cell approximation for fuel assembly, (ii) simplified ring model, and (iii) detailed ring model for all reactor core modeling including fuel assemblies, inner and outer reflectors, core barrel, and ractor pressure vessel (RPV). All three approaches include the lower and upper plenum, heat exchanger and blower components for primary loop simulations.

2.2 Modeling and Simulations of MHTGR using the Unit Cell Core Model

In SAM, PBCoreChannel component was selected to model both coolant channel and heat structures in the unit-cell core model. It uses one average fuel-block coolant-channel cell to represent the active core. The primary loop geometry consists of upper and lower plenum, coolant channels, heat exchanger and blower configuration as shown in Figure 3i. To simulate a fuel assembly, the required information for this component includes heat structure thickness, coolant channel hydraulic diameter, total coolant channel cross section area, length of the core, heat surface area density, power distribution, and number of fuel rods. Initial and operating conditions are specified in Table 3.

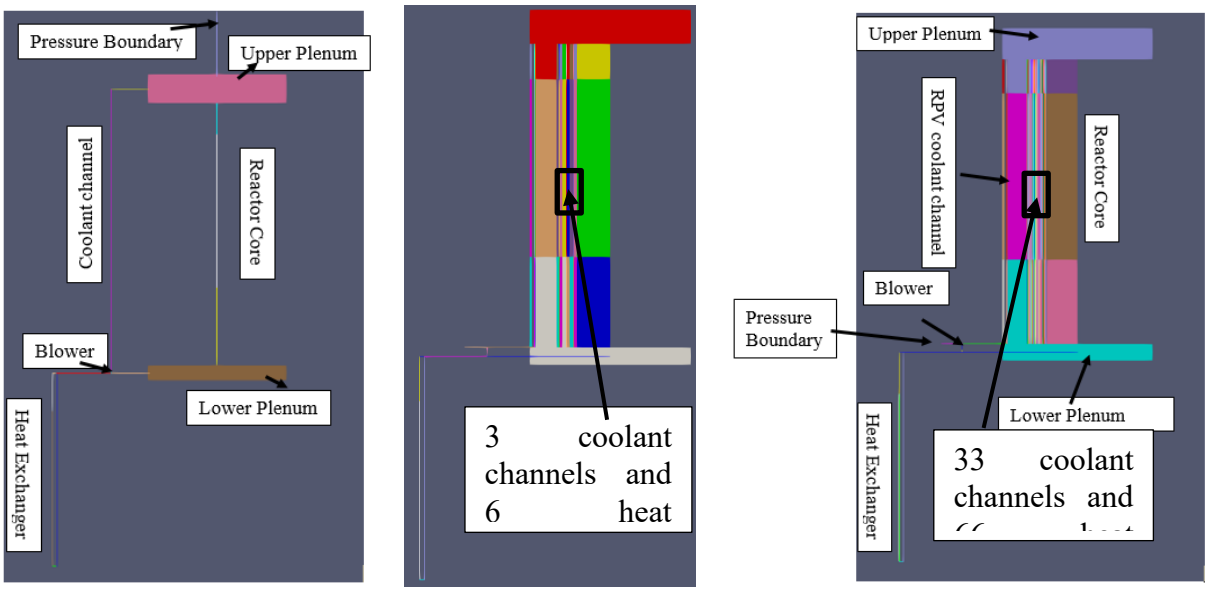

(i) (ii) (iii)

Figure 3. SAM models, (i) Block-chanel, (ii) simplfied ring and (iii) detailed ring.

The MHTGR primary loop results were based on transient solver. An increase of coolant temperature and velocities from the top to the bottom of the reactor were due to forced circulation flow which drives the fluid flow from the upper to the lower plenum. Similarly, the temperature increase was observed in heat structures towards the lower plenum (Figure 4). The hot coolant from the lower plenum was cooled in the heat exchanger before it is sent to the blower. The blower drives the riser flow in a RPV coolant channel which was located between the reactor pressure vessel and core barrel and it was connected with the upper plenum.

As seen in Table 4, the SAM code simulation results for normal operation conditions were almost identical to the MHTGR design conditions. It is also noted that the maximum temperatures for both coolant and heat structures were well below the specified design limits.

To examine the code capabilities and performance, power operation transient simulations were performed with specified time histories of power, pump head, and heat exchanger secondary coolant mass flow rates, as shown in Figure 5.

Table 3. MHTGR operating conditions [2]

Pressure [MPa]	7.0
Inlet core temperature [K]	623.15
Outlet core temperature	1023.15
Mass flow rate in core [kg/s]	289.13
Total core flow area [m^2]	2.06
Fuel thickness [mm]	2.065
Graphite thickness [mm]	0.465
Clad thickness [mm]	0.52
No. of fuel rods	21420
Active core height [m]	7.93
Upper support heat structure [m]	1.617
Lower support heat structure [m]	4.04
Heated surface area density [1/m]	199.3
Mass flow rate per channel [kg/s]	0.0278
Velocity [m/s]	26.19
Reynolds number	1.38E+05
Power [MW]	600

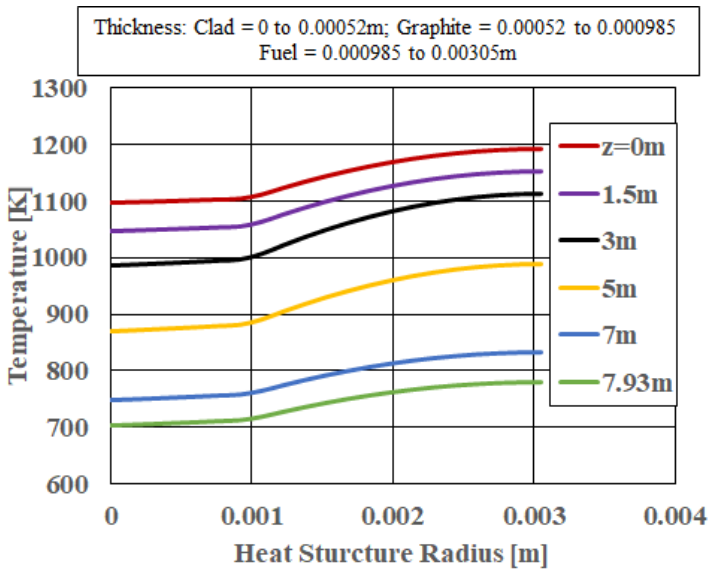

Figure 4. Solid temperature radial distribution at various axial location in a primary loop.

Table 4. SAM simulation results at normal operation conditions

Parameters	Simulation results	Design conditions
Inlet Core Temperature [K]	623.14	623.15
Outlet Core Temperature [K]	1023.26	1023.15
Pump flow rate [kg/s]	289.05	289.1
Upper Plenum Temperature [K]	623.14	623.15
Lower Plenum Temperature [K]	1023.26	1023.15
Heat Exchanger Primary Outlet Temperature [K]	623.14	623.15
Peak Fuel Temperature [K]	1191	-
Peak Clad Temperature [K]	1101.5	-
Peak Graphite Temperature [K]	1105.3	-

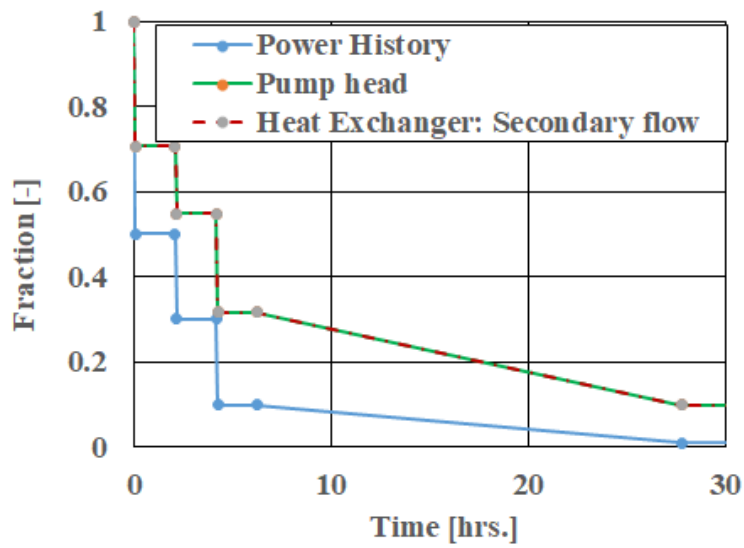

Figure 5. Controlled reactor transient profiles for power, pump head and heat exchanger secondary flow

SAM simulation results of power transients are shown in Figure 6. The maximum temperature drops were observed up to ~0.1 hr due to the much reduced power level but relatively higher flow rates in both the primary loop and the secondary side of the heat exchanger. The moderate increase was observed between ~0.1 hr and ~4.2 hrs where the increase of power to flow ratio during the time period. Furthermore, the significant increase was observed from ~4.2hrs onwards. The temperature jump at 4.2 hrs was mainly due to increased ratio of reactor power to flow ratio, and the reactor power to heat exchanger removal ratio. The velocity drop (Figure 6iii) is in line with the specified profiles in Figure 5.

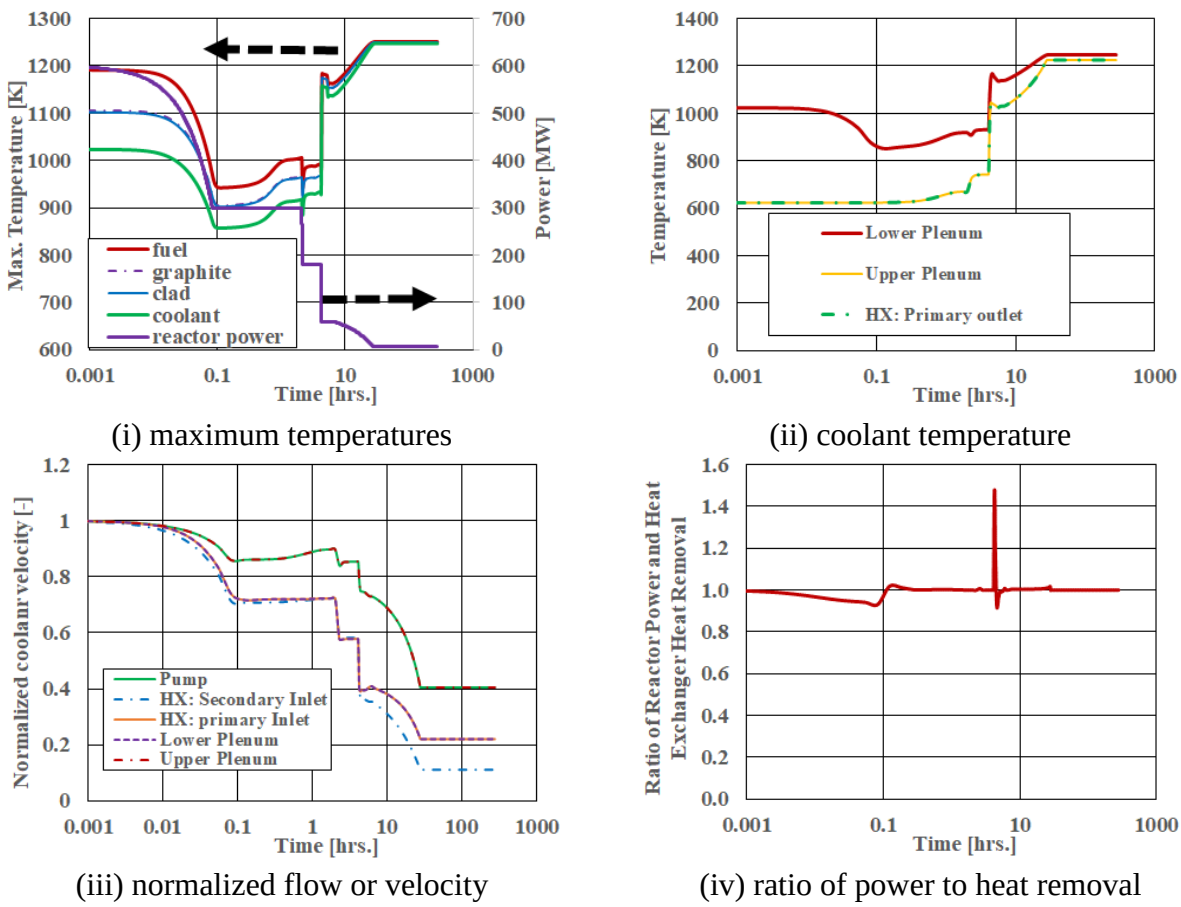

(i) maximum temperatures (ii) coolant temperature

(iii) normalized flow or velocity (iv) ratio of power to heat removal

Figure 6. SAM simulation results of power transients

2.3 Modeling and Simulations of MHTGR using SAM Ring Model

The detailed MHTGR model was developed in SAM using a ring approach based on a specified coolant channel pitch of fuel assembly. The detailed ring model includes all components; upper and lower plena, coolant channels, heat structures (fuel, reflectors, RPV, core barrel and RCCS) including heat exchanger and forced circulation flow (blower). In Figure 3iii, the SAM simulated geometry is shown for MHTGR primary loop. In this model, each ring of fuel assemblies is represented by 11 coolant channels and 22 heat structures.

In SAM, the coolant channels and the heat structures were modeled with 1-D and 2-D components, respectively. In the reactor core, the power distribution profile was specified. In the SAM model, the homogenized assumption was considered for fuel ring heat structures. The geometry details and operating conditions were provided in Tables 1 and 2. The flow and heat structures names were defined in Table 5.

In SAM, temperatures between heat structure surfaces are communicated by providing a gap heat transfer coefficient. In this work, the gap heat transfer coefficient was assumed to be 10^7 to avoid any discontinuities. On the other hand, the RCCS was modeled via radiation heat transfer between the reactor pressure vessel and RCCS. From the RCCS, the heat was rejected to ambient air with a provided convective heat transfer coefficient of 19.74 W/m^2-K.

Two SAM simulations for the MHTGR were performed with the detailed ring model, including the normal operating conditions and reactor transient simulation under the PCC event.

Table 5. The flow and heat structure names

Inner reflector	R-1
Inner fuel ring left structure	R-2-L(11)
Inner fuel ring fuel ring coolant channel	R2-Channel (11)
Inner fuel ring right structure	R-2-R (11)
Middle fuel ring left structure	R-3-L (11)
Middle fuel ring fuel ring coolant channel	R3-Channel(11)
Middle fuel ring right structure	R-3-R(11)
Outer fuel ring left structure	R-4-L(11)
Outer fuel ring Fuel ring coolant channel	R4-Channel(11)
Outer fuel ring right structure	R-4-R(11)
Outer reflector	R-5
Core barrel	R-6 (core barrel)
Coolant channel	R-6C (coolant)
Rector pressure vessel	R-7 (RPV)
Reactor cavity cooling system	RCCS

In Figures 7 and 8, the increase of coolant and solid temperatures in the bottom of the reactor were mainly due to the forced circulation flow from upper to lower plenum. The hot coolant from the lower plenum was cooled in a heat exchanger before it sends to blower. The blower drives the flow towards an upper plenum via RPV coolant channel which was located between reactor pressure vessel and core barrel. Similarly, the velocity increase was observed in coolant channels towards the lower plenum due to the density drop.

In Figure 8, the coolant temperature and velocities are shown for one of the coolant channels from out of 11 from each fuel assembly. To be noted, the results are shown for external coolant channel in each fuel ring. The velocity and temperature increases were observed towards the bottom of the active core as expected. In a RPV coolant channel, the change of temperatures and velocities were minimal (R6_C).

In Figure 9, the change in solid temperature was minimal in the inner reflector and fuel rings from 0m to 2.41m. A significant temperature drop was observed in the outer reflector, core barrel, reactor pressure vessel, and RCCS riser walls. The heat removal through the RCCS was approximately 1.05 MW under normal operating conditions. To be noted, the RCCS was modeled based on radiation heat transfer between RPV and RCCS heat structures. In the RCCS, the heat was rejected to ambient air with a provided convective heat transfer coefficient of 19.74 W/m^2-K.

Simulations were also performed under an accident scenario. The converged results from normal operating conditions were used to run reactor transients with a specified power history profile (Figure 10 [3]). To be noted, both heat exchanger and blower performance were assumed complete failures (zero pump head and zero heat removal) to study the reactor performance.

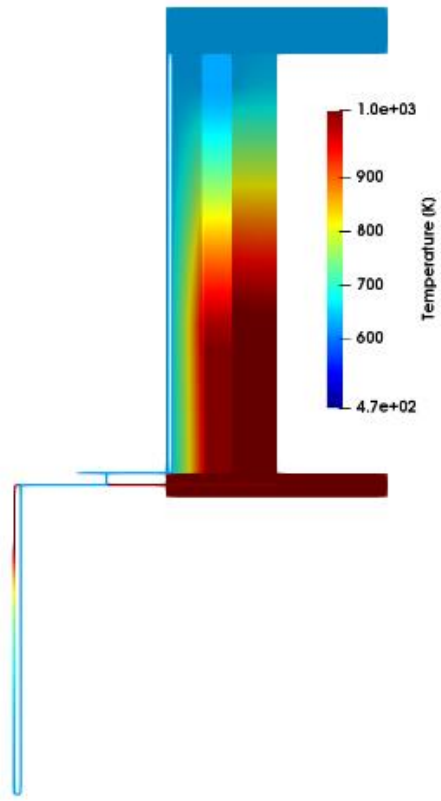

Figure 7. Fluid and solid temperature distribution

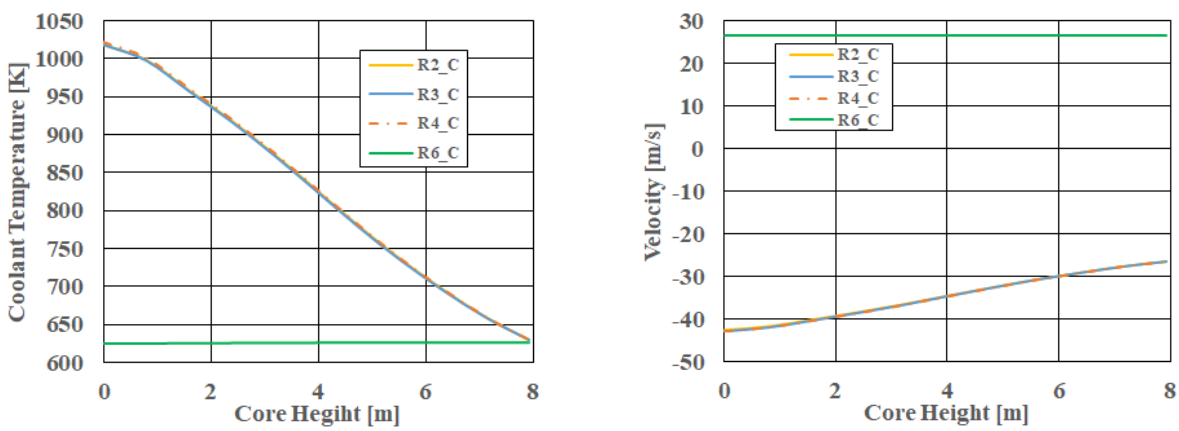

(i) Temperature (ii) Velocity

Figure 8. Coolant temperature and velocity distributions in the active core

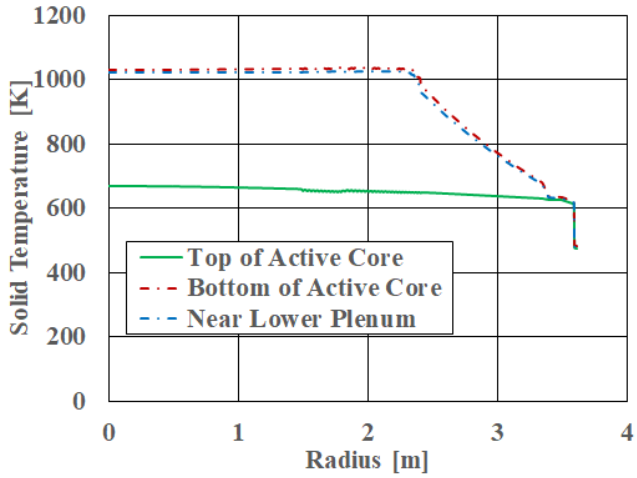

Figure 9. Heat structure temperature across radial direction

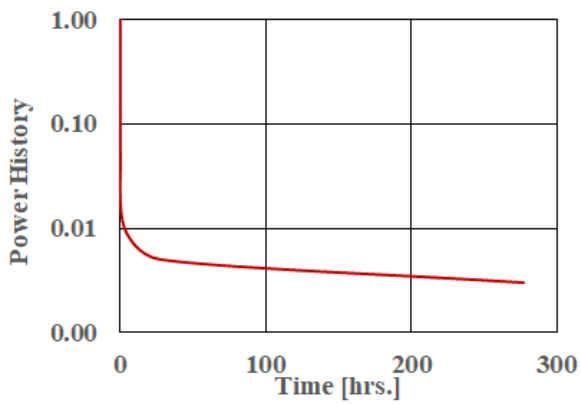

Figure 10. Power History for accident scenario.

From Figure 11, the significant temperature increase was observed in fuel rings, which was still under the design limits. To be noted, the maximum temperature plot was shown only for the outer most heat structure in each fuel ring (inner, middle and outer). The details of the maximum values within the reactor are shown in Table 6. The reactor core temperatures significantly increased within five hrs of reactor shut down. On the other hand, the moderate increase of heat structure temperatures was observed for the outer reflector, core barrel, RPV and RCCS. The calculated maximum heat removal was about 3.15 MW from the RCCS (Table 6).

In the upper plenum, the coolant temperature increase was observed with an increase of time due to loss of forced circulation flow (Figure 12i). In contrast, the coolant temperature in the lower plenum decreased right after the transient started (t=0). Figure 12 also shows the coolant velocities for the pump and heat exchanger. Natural circulation flow was observed due to buoyancy driven flow.

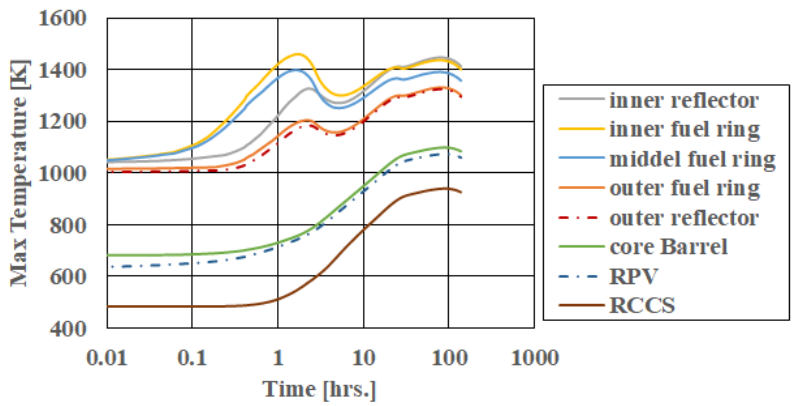

Figure 11. Heat structures maximum temperatures.

Table 6. Compassion of maximum values for reactor transients with normal operating conditions

	Normal	**PCC**
Inner reflector [K]	1043.22	1446
Inner fuel ring [K]	1042.3	1459
Middle fuel ring [K]	1038.8	1397
Outer fuel ring [K]	982.9	1390
Outer reflector [K]	981.47	1292
Core Barrel [K]	678.8	1098
RPV [K]	633.5	1073
RCCS [K]	482.9	939
RCCS heat removal [MW]	1.048	3.15

The flow direction was changed from downward to upward in the reactor core due to loss of forced circulation flow. However, inside the reactor, the outer fuel ring showed downward flow due to lower temperatures (Figure 13) compared to the inner and middle rings (Figure 14). Hence, the internal (parallel channel) flow circulation was established in the reactor core. In Figure 14, the coolant temperature profiles were shown for one of the outer coolant channel from inner, middle and outer fuel rings. Also, the bypass coolant channel was shown in Figure 14(iv). At top of the active core, the increase of temperature was due to natural circulation flow, as discussed above. Moreover, the temperature magnitudes drop towards the outer fuel rings.

As seen in Figure 15, the heat removal from RCCS increased up to 94 hrs. Further increasing the time, the heat removal drops due to the decrease in the vessel wall temperature. The maximum heat removal was calculated around 3.15 MW from RCCS (Table 6), although the heat removal surpassed the reactor power at around 28 hrs.

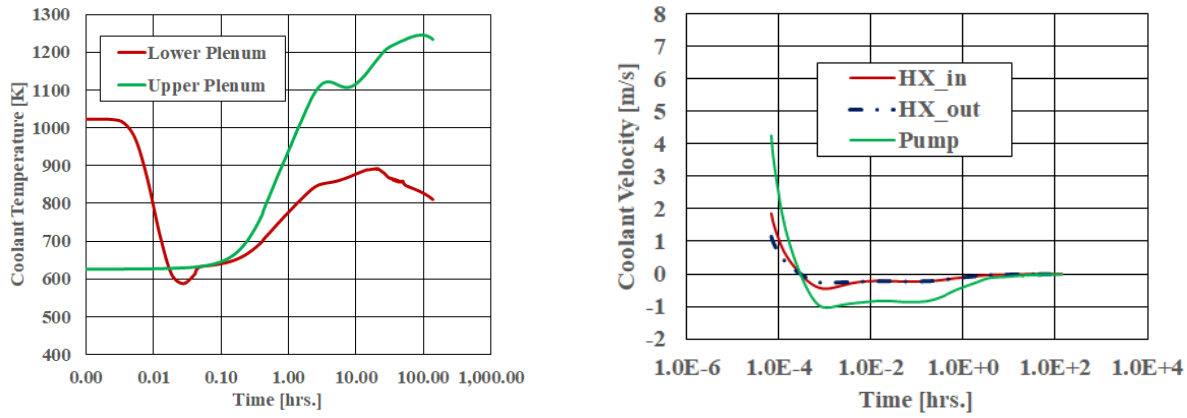

(i) temperatures (ii) velocity

Figure 12. Coolant temperatures and velocity during the PCC transient

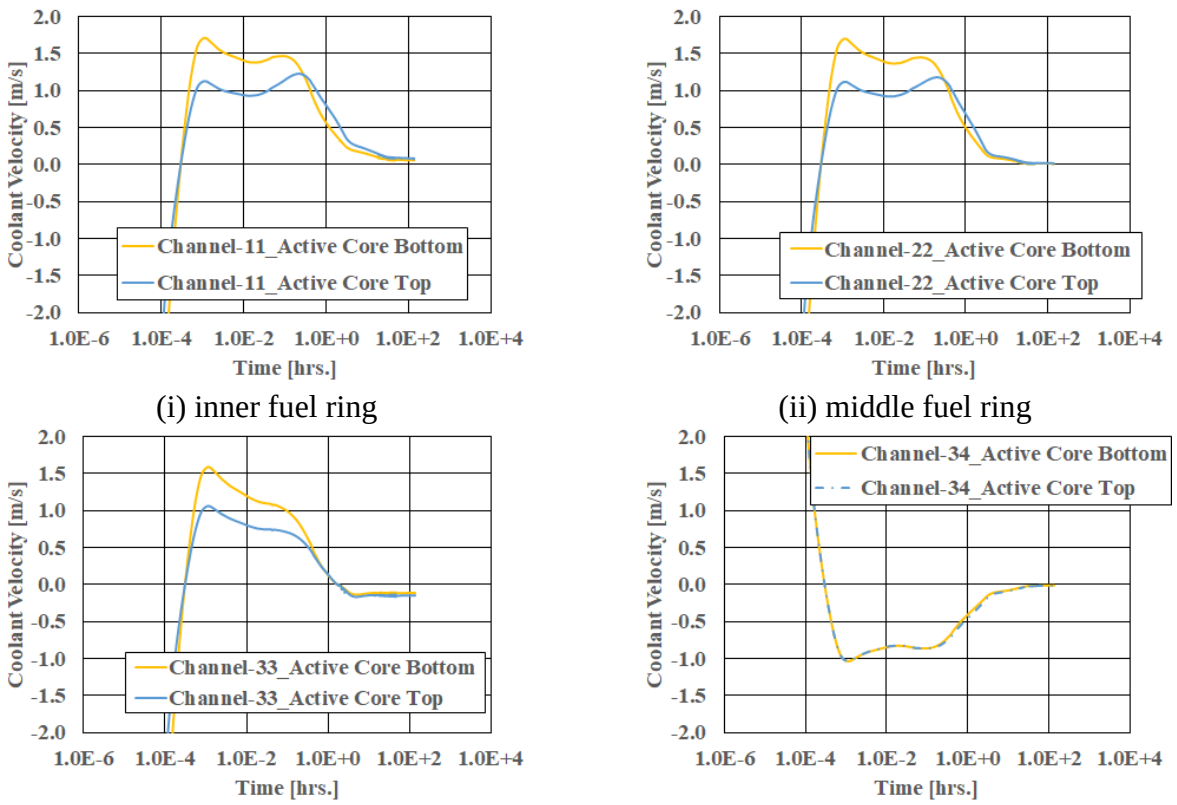

(i) inner fuel ring (ii) middle fuel ring

(iii) outer fuel ring (iv) RPV

Figure 13. Coolant channel velocities during the PCC transient.

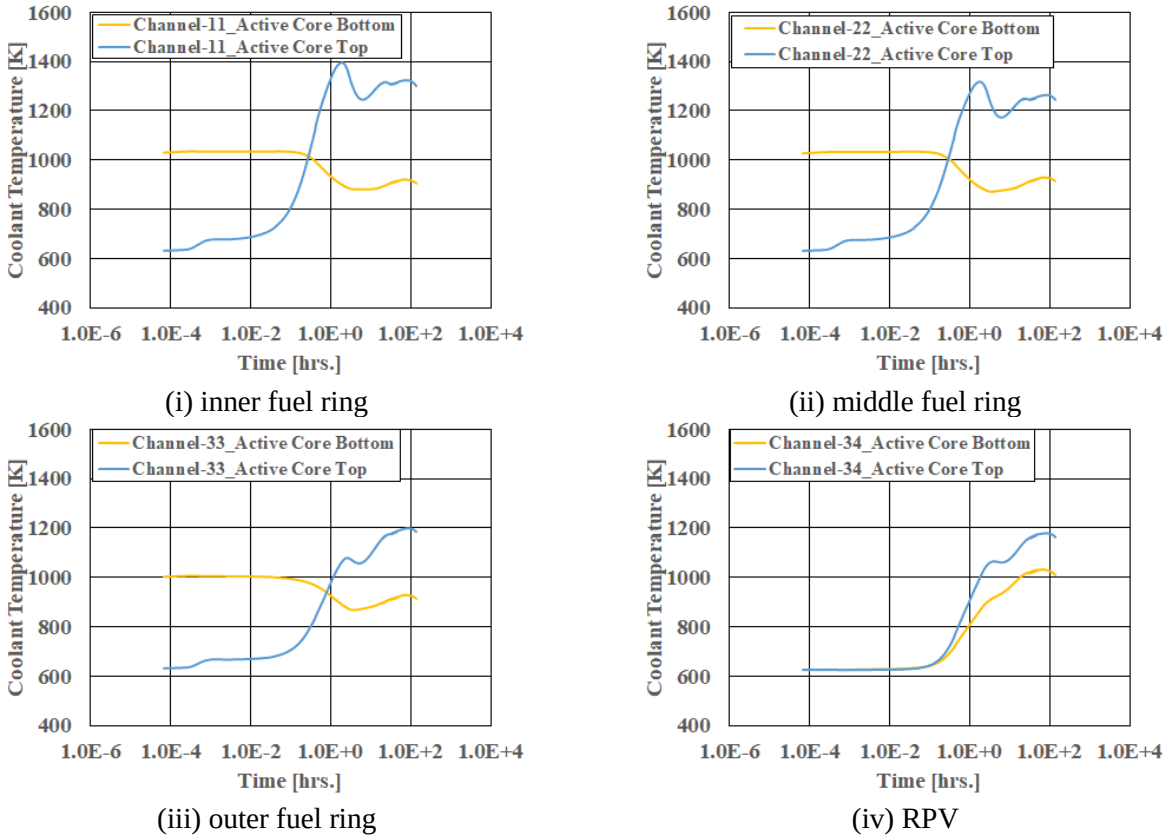

Figure 14. Coolant channel temperatures during the PCC transient.

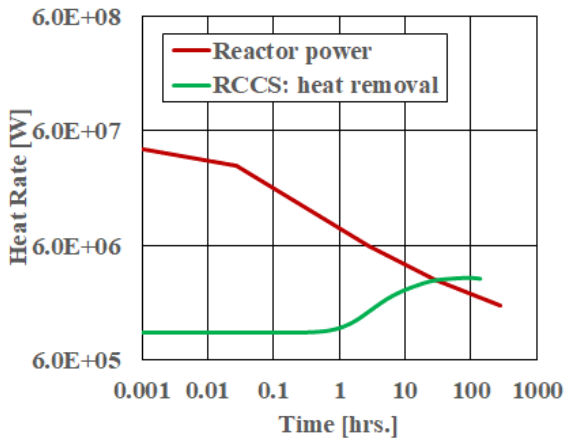

Figure 15. RCCS heat removal and reactor power

2.4 Conclusions

A standard SAM HTGR problem was developed in this work based on GA's MHTGR design to assess SAM code capabilities for the primary loop simulations of HTGR. It is noted that integral-effects standard problems are foundational to the methodologies employed by the industry user community to verify the adequacy of computer codes and evaluation models. Two models were developed in SAM to simulate the reactor core, i.e.: unit cell approximation or detailed ring model. Both approaches include the lower and upper plena, heat exchanger, and blower components for primary loop simulations. In both approaches, the coolant channels and the heat structures were modeled using 1-D and 2-D components, respectively.

Under normal operating conditions, the SAM calculated results for coolant and heat structure temperatures and coolant velocities were within the reactor designed limits. The calculated RCCS heat removal was around 1.048 MW. Under the pressurized conduction cooldown accident scenario, the SAM calculated results for coolant and heat structures temperatures were still within the designed limits. The significant increase of reactor core temperatures was found within 5 hrs of reactor shut down. The natural circulation flow was observed in the primary loop as well as inside the reactor core, due to the much lower temperatures in the outer fuel rings than in the middle and inner fuel rings. The calculated maximum RCCS heat removal was around 3.15 MW, about three times of heat removal at normal operating conditions.

No obvious gaps in code capabilities were identified for the two test cases: power transient and pressurized conduction cooldown event. It is confirmed that the SAM simulations using the detailed ring model can accurately model the convection-dominant in-core heat-removal during normal operating conditions and conduction-dominant heat-removal during PCC transient conditions. On the other hand, the single-channel unit-cell approach is appropriate for convection dominant regime simulations because of its superior execution speed.

Potential future model improvement includes the simulations of heat structures within the fuel assembly for graphite, cladding, and fuel to avoid homogeneous assumption for fuel assemblies, and the explicit modeling of the RCCS air natural circulation flows. Additionally, coupled multi-scale multi-physics simulations can be pursued with using SAM for primary loop simulation, Pronghorn for full 3D vessel simulation, RELAP-7 for the steam generator and Rankine cycle simulation.

3. Kairos Project

Molten salt reactors and their variants are currently an attractive option in the private energy sector. The variant being considered by Kairos Power LLC is the fluoride-cooled high temperature reactor (FHR). In this design, fluoride-based molten salt acts as the coolant flowing through a bed of graphite pebbles which contain TRISO fuel particles. This design provides several advantages as it allows the coolant to reach high temperatures, increasing the overall plant efficiency, and operate at near-atmospheric pressure.

The design of the FHR core calls for the pebble bed to be surrounded by a neutron reflector made of graphite blocks. The objective of this work is to evaluate coolant flow through the gaps between the graphite blocks in order to determine if this flow could be a potential issue for the reactor design. It is expected that the flow from the core into the bypass through the reflector blocks is small, however this must be quantified. The models and methods used to simulate this flow are outlined and the results of initial testing via a parametric study are presented.

3.1 Problem Description

A pebble bed core in an FHR is surrounded by a neutron reflector. In one proposed design, the reflector is composed of solid graphite blocks which are fit together. Between the graphite reflector and the core barrel there is a bypass channel. Due to the flow blockage caused by the pebbles in the core, the pressure drop through the core region is expected to be high. In the bypass channel, outside of the reflector, there is no flow blockage and the anticipated pressure drop is expected to be much lower compared to the core. This can lead to a significant pressure difference between the core and the bypass channel, across the graphite reflector blocks. Despite fitting together relatively well, there will still be cracks and gaps between blocks and this pressure difference will drive some amount of flow from the reactor core into the bypass channel, or potentially, under certain conditions, in the opposite direction.

A simplified model of the reactor core, graphite reflector, and bypass channel has been developed. The model represents a small section of the full system geometry. The core, reflector and bypass channel can be reasonably represented by concentric circular regions. The model consists of a 15° azimuthally symmetric and axially periodic section of these regions, shown in Figure 16 with associated dimensions provided in Table 7. The core region is depicted in red, with the gaps between the graphite blocks in green, and the bypass channel in blue. Only a relatively small section of the core region was included as the flow distribution in this region is nearly uniform and the additional complexity would have little effect on the results of the study.

3.2 Nek5000

Nek5000 is the NEAMS CFD tool for high-fidelity simulation of fluid flows [5]. It is based on the spectral element method, a subset of the finite element method. Nek5000 solves the conservation of mass, momentum, and energy equations on a mesh of high-order conformal hexahedral elements which are discretized in space using Gauss-Lobatto-Legendre (GLL) quadrature. The conservation of mass equation can be formulated using a low-Mach approach, which accounts for changes in density with respect to temperature. In the approach used in this work, density was assumed to be constant (incompressible flow) and the conservation of mass equation is given as the divergence-free constraint

$$\nabla \cdot \boldsymbol{u} = 0 \tag{1}$$

The conservation of momentum equation accounts for the acceleration of the fluid. It is implemented in Nek5000 in the following form

$$\rho\left(\frac{\partial \boldsymbol{u}}{\partial t} + \boldsymbol{u} \cdot \nabla \boldsymbol{u}\right) = -\nabla P + \nabla \cdot \mu[\nabla \boldsymbol{u} + (\nabla \boldsymbol{u})^T] + \rho \boldsymbol{F} \tag{2}$$

Note the inclusion of a body force term, which is used to include a porous media model. The body force due to gravity was neglected. For constant density flows, this has no effect on the solution.

3.3 Porous Media Model

Flow through the pebble bed core is simulated using a porous media model. This is incorporated as a body force in the momentum equation,

$$\boldsymbol{F} = -\frac{\nu}{\varepsilon}\boldsymbol{u} \tag{3}$$

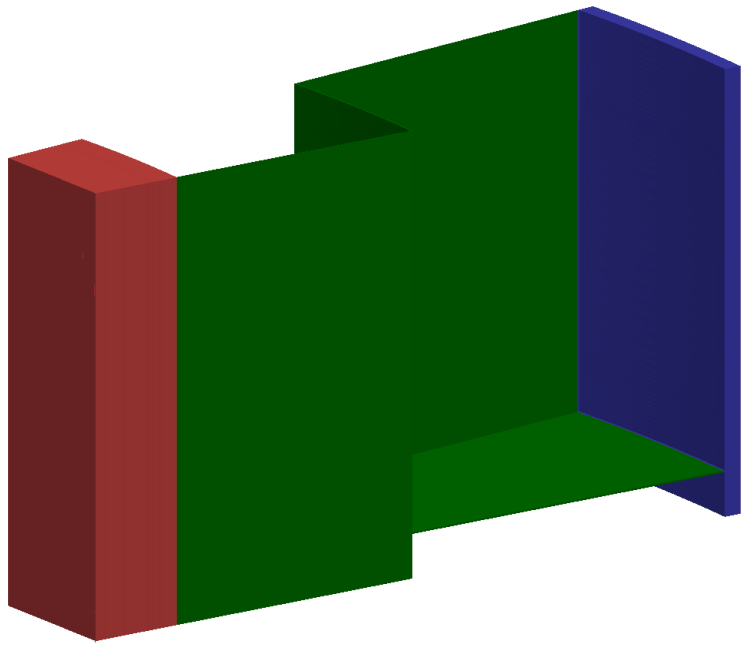

Figure 16: 3D model of a 15° wedge shaped section of the FHR core-system with the core region shown in red, gaps between graphite blocks in green, and the bypass region in blue

Table 7: Reference dimensions for the bypass flow geometry

Dimension	Value
Core region radius [cm]	260
Graphite block thickness (inner layer) [cm]	30
Graphite block thickness (outer layer) [cm]	40
Gap thickness [cm]	0.2
Bypass flow channel thickness [cm]	2
Total height [cm]	50.2
Pebble diameter [cm]	3

where the permeability is calculated from the Carman-Kozeny correlation [6]. This force was only included in the core region (the red region in Figure).

$$\varepsilon = \frac{D_{peb}^2 \phi^3}{180(1-\phi)^2} \tag{4}$$

For the value of porosity assumed for the 3 cm diameter pebble bed, this yields a permeability of $8.89(10^{-7})$ m^2. The permeability was increased near the wall following a parabolic profile within 5 cm of the graphite reflector and was done for stability and to mimic the physical effect of the wall on the distribution of pebbles, as they do not pack as tightly near the wall. This represents a narrow region and

should have only minor effects on the overall results. To confirm that it has a small effect, the expected pressure drop in the core region can be calculated from Darcy's law for porous media

$$\Delta P = \frac{\mu}{\varepsilon} H \tag{5}$$

where H is the total height of the core region. This is used as a point of comparison for the simulations.

3.4 Results

In order to evaluate the flow through the gaps between reflector blocks, a parametric study was performed. The flow rate through the reactor core was held constant based on the expected design specifications, while the flow rate through the bypass region was varied by controlling the ratio of mean velocity between the core and the bypass region. For an incompressible flow, this corresponds to varying the mass flux by the same ratio. Three values were tested: 1%, 5%, and 10%. This covers a relatively wide margin as the uncertainty in the expected flow rate through the bypass region is large. The reference parameters for all three simulations are presented in Table 8 along with the anticipated pressure drop through the core region as predicted by Eq. (5). Reference Reynolds numbers are provided for the core overall, as well as for a single pebble.

The inlet to the core region was prescribed with a constant velocity which was blunted very close to the graphite block reflector to accommodate the no-slip wall boundary condition on the graphite blocks. The three sides of the core region that were not on the graphite blocks were prescribed as symmetry boundaries. In the bypass region, a parabolic inlet velocity profile was prescribed. Outlet boundaries were prescribed at the tops of both the core and bypass region. The bypass region was bound by symmetry boundaries in the azimuthal direction and no slip walls in both radial directions, except where intersected by the gaps. The top and bottom boundaries of the gap region were prescribed as frictionless walls (symmetry).

Table 8: Reference conditions for the parametric study

Parameter	Value
Density [kg/m^3]	2011
Viscosity [kg/m-s]	0.01069
Total mass flow rate through the core [kg/s]	1450
Mass flux through the core [kg/m^2-s]	273
Mean (superficial) velocity through the core [m/s]	0.14
Darcy velocity through the core [m/s]	0.34
Porosity	0.4
Permeability [m^2]	8.89 (10^{-7})
Correlated pressure drop (Eq. (5)) [Pa]	845
Reynolds number (core)	66,000
Reynolds number (pebble)	1920

In the spectral element method, the solution to the governing equations is approximated over an element using a polynomial approximation in space. The order of the polynomial approximation is directly related to the resolution of the solution. The error related to the spatial approximation decreases exponentially with increasing polynomial order. This is compared to algebraic or linear convergence with increasing element discretization. Mesh resolution studies can be performed using either method, the former known as a p-type study with the latter known as an h-type. For this work, results were tested for mesh independence using a p-type study with approximation orders of 5 and 7. Little to no difference was observed in the results and it was determined that a 5th order approximation was sufficient.

The complete 3D mesh used is shown in Figure 17(a). A simple block mesh was originally developed. However, the gaps were meshed using a minimum of three elements across. This led to unnecessarily fine regions and put undue restrictions on the time step due to the Courant-Friedrichs-Lewy (CFL) constraint. This was mitigated by performing manual mesh smoothing. The GLL points were displaced in the axial direction with a hyperbolic tangent function, with larger displacements farther away from the graphite blocks. The effect of this displacement can be seen in Figure 17(b). This resulted in a significant relaxation in the severity of the CFL constraint.

The pressure distribution for the 5% bypass flow case is presented in Figure 18. The other two cases showed similar distributions. As expected, the porous media model results in a significantly greater pressure drop through the core region compared to the bypass region. It can be seen from the figure that the pressure drop through the bypass region is practically negligible compared to the core region. The total pressure drop through the core region is predicted by the Nek5000 model as about 902 Pa. This compares reasonably well with the results from the correlation represented by Eq. (5) and indicates that the porous media model has been implemented consistently.

In the gap immediately adjacent to the core, the pressure is still observed to be quite high. This dissipates quickly along the gap as the gap is narrow and has a significant flow resistance. By the time the flow has reached the outer side of the first graphite block, the pressure has decreased by 90%.

The radial velocity distribution for the 5% bypass flow case is presented in Figure 19. Again, this represents a typical distribution for all three cases. From the figure, the velocity is highest in the gap between graphite blocks near the core inlet, where the pressure differences is greatest. It is worth noting that the radial velocity is practically zero throughout the core region. As expected, along the axial direction, as the pressure difference between the core and the bypass region drops, the radial flow decreases significantly.

Two dimensional slices of the radial velocity through the lower horizontal gap are shown in Figure 19. This shows the overall flow distribution through a region where the pressure difference between the core and bypass channel is still quite high. The complete slice is shown in Figure 20(a), which shows the coolant initially flowing outward quickly from the high pressure core region then slowing as it spreads through the vertical gap. It can also be seen that there is some radial flow in the core region with the coolant moving towards the reflector.

A zoomed in section of the junction between the core region and the vertical gap is shown in Figure 20(b). Flow in this region behaves similarly to flow between parallel plates, except the flow is non-uniform along the vertical direction. Despite this difference, a parabolic velocity profile quickly develops. This indicates that the flow losses in this region could potentially be well captured using a reduced order model. The flow can also be seen to decrease in radial velocity even in the short section shown. This may introduce a level of complexity when trying to develop a reduced order model to capture these phenomena.

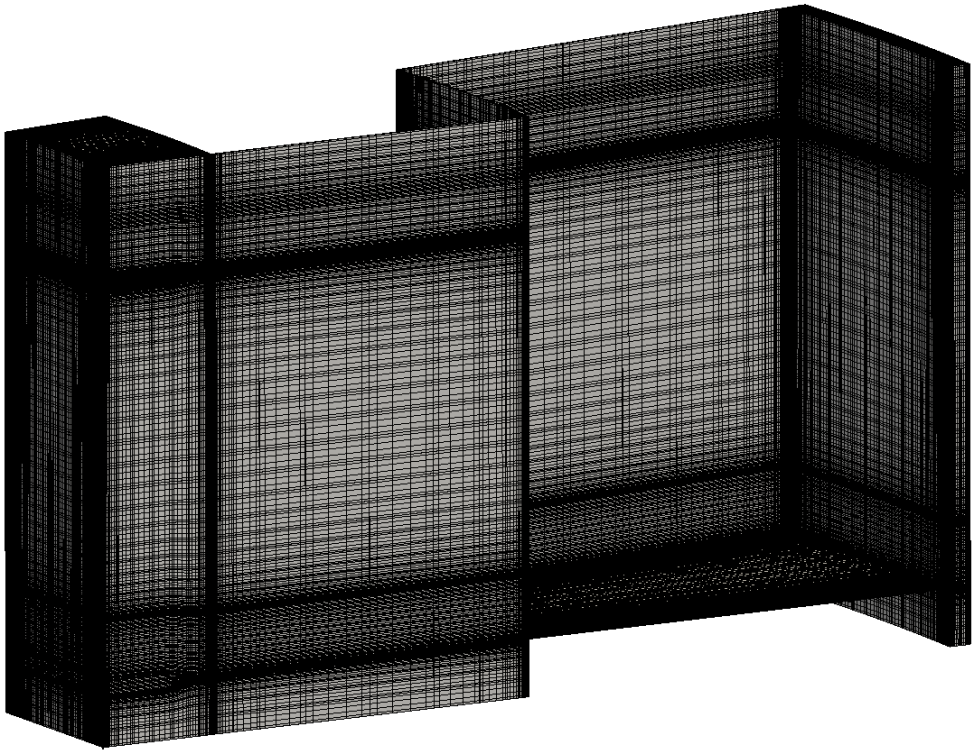

(a) complete 5th order mesh

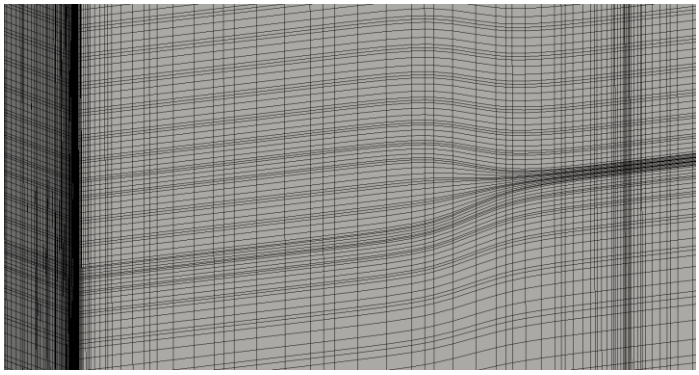

(b) zoomed in region showing modification

Figure 17. Computational mesh used to simulate the flow showing (a) the complete mesh with GLL quadrature and (b) a zoomed in region near a location where the mesh was modified

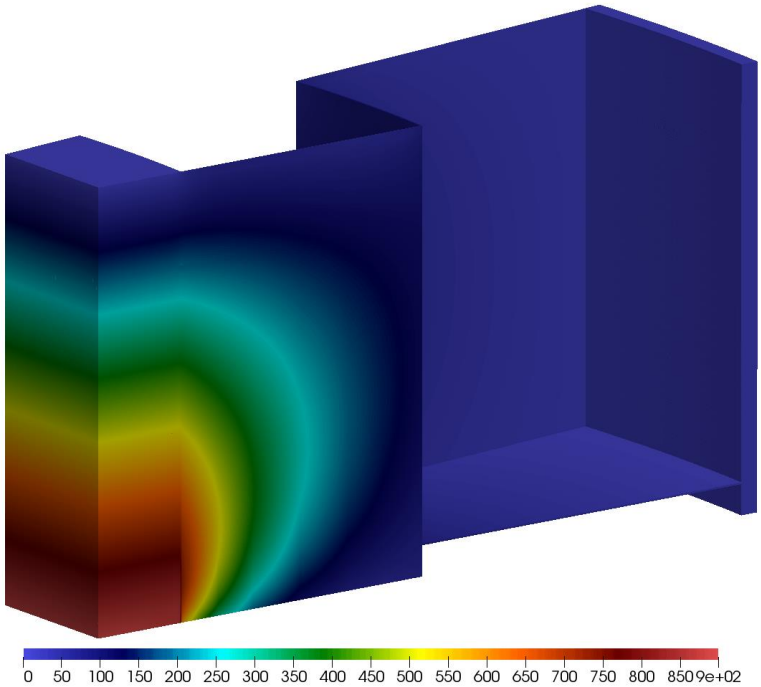

Figure 18: Pressure (Pa) distribution in the 3D domain

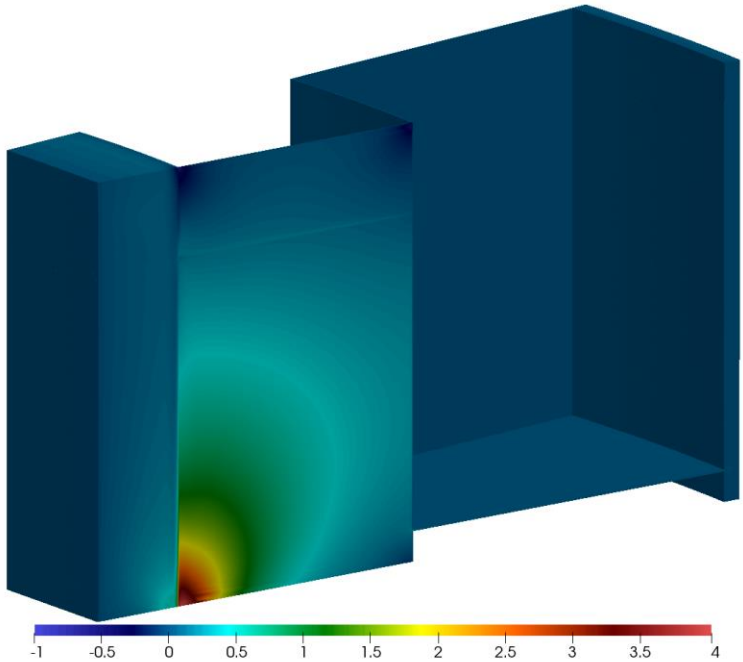

Figure 19: Radial velocity (m/s) distribution in the 3D domain

(a)

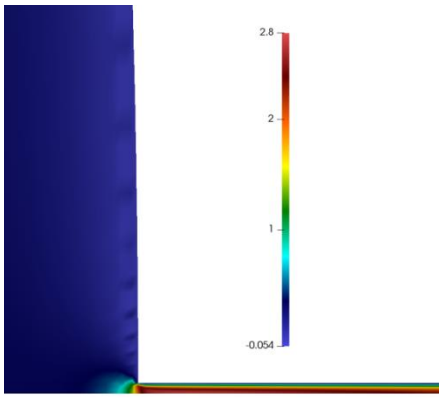

(b)

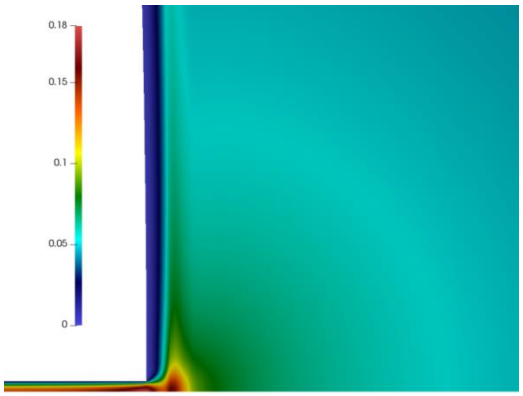

(c)

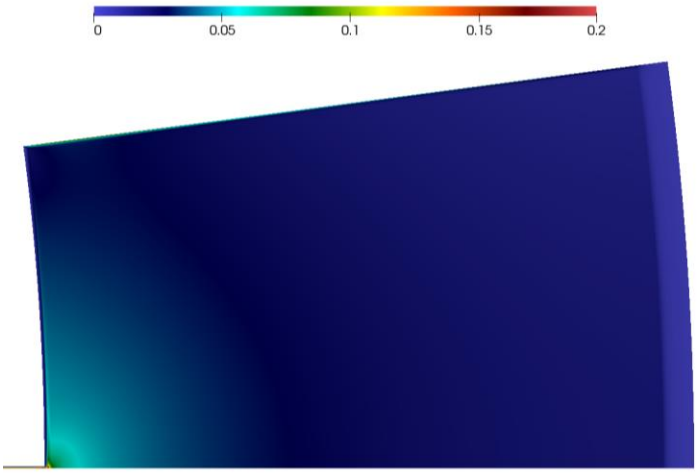

(d)

Figure 20: Details of radial velocity (m/s) on a slice through the domain aligning with a horizontal gap in the graphite reflector blocks showing (a) the complete slice, (b) the transition from the core to a vertical cap, (c) the transition from a vertical gap to a horizontal gap, and (d) the horizontal gap

A zoomed in section of the junction between a vertical gap and a horizontal gap is shown in Figure 20(c). The flow can be seen to exit the vertical gap with peak velocity of around 0.18 m/s. This is a significant decrease compared to 2.8 m/s at the junction between the core and the vertical gap. However, it is still relatively high compared to the remainder of the horizontal gap. The trend of slowing velocity is seen to continue as the flow spreads through the horizontal gap.

Figure 20(d) shows a zoomed in cross section through the horizontal gap between the graphite blocks in the outer ring. This shows the radial velocity continuing to decrease as it moves towards the bypass region. In fact, in most of the horizontal gap the radial velocity is practically negligible.

The mass flow rate leaving the core region and flowing through the gaps between the graphite neutron reflector blocks was determined by integrating the local mass flux over the outflow boundary for just the core region. Similarly, for the bypass region the total mass flow rate through the outflow boundary was also calculated. These two numbers were compared to ensure consistency. The value obtained for the 15° wedge section was then scaled to account for a full 360° system. The total mass flow rate leaving the core region is presented Figure 21 for each of the three parametric cases presented as a fraction of the total flow rate through the core as a function of the velocity ratio (or mass flux ratio) between the bypass and the core region. It can be seen from the figure that the total mass flow lost from the core region decreases as the flow rate through the bypass region increases. This is expected, as the higher flow rate through the bypass region leads to a higher pressure drop in the bypass region, resulting in a lower pressure difference between the core and the bypass region. However, this effect is very small, as increasing the bypass flow rate from 1% to 10% resulted in a practically negligible change in the total lost mass flow rate.

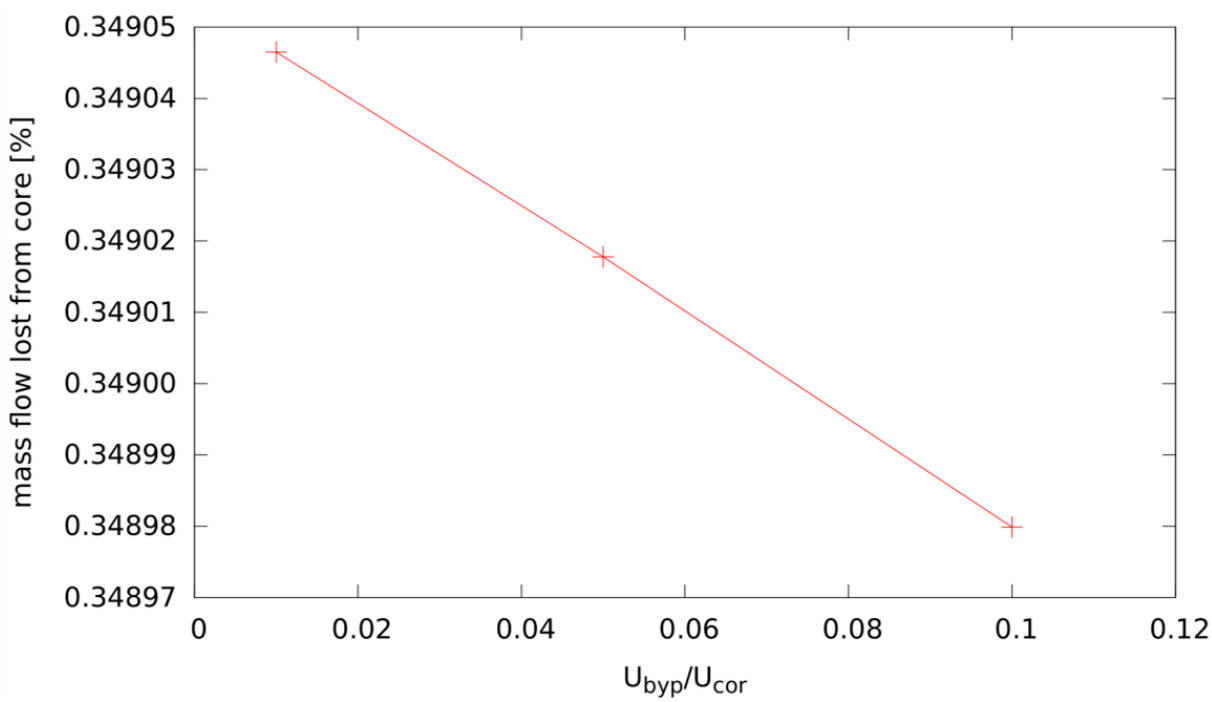

Figure 21: Mass flow rate leaving the core through the gaps in the graphite blocks as a percentage of total mass flow through the core

3.5 Summary and Conclusions

Nek5000 has successfully been applied to perform a parametric study for coolant flow lost through gaps between graphite blocks forming the neutron reflector around a pebble bed FHR core, with a porous media model implemented and used to simulate the flow through the pebble bed core. Some issues in stability were encountered in implementing the porous media model. However, these were overcome with only minor modifications.

The flow leakage from the core region was shown to decrease as the flow rate through the bypass region was increased. This was due to the associated decrease in pressure difference across the reflector blocks. However, for the tested conditions the flow resistance of the gaps between graphite blocks was the dominant factor and the rate of flow leakage varied practically insignificantly. Overall, the total mass flow rate lost through the simulated section of the core was small for all cases, on the order of 0.35%.

The suggested next steps for this study would be to expand the simulations to account for a larger core region, perform cross code comparisons to ensure the consistency of the results, and to further refine the porous media implementation in Nek5000 to be more robust.

References

1. R. Hu, SAM Theory Manual, Argonne National Laboratory, *ANL/NE-17/4* (2017).
2. HTGR technology course for the nuclear regulatory commission. Module 5a, "Prismatic HTGR core design description". Idaho National Laboratory, *May 24-27, 2010*. https://art.inl.gov/NGNP/INL%20Documents/NRC%20Training%20Presentations/Module%2001%20-%20Introduction.pdf
3. Decay heat removal and heat transfer under normal and accident conditions in gas cooled reactors. *IAEA-TECDOC-757, ISSN 1011-4289*, Proceedings of a specialists meeting, Julich, Germany, 6-8 July 1992.
4. G. Strydom et al., "Comparison of the PHYSICS/RELAP5-3D ring and block model results for phase I of the OECD/NEA MHTGR-350 benchmark, *Nuclear Technology, Vol 193, 15-35, 2016.*
5. Fischer, P. F., Lottes, J, Pointer, W. D., and Siegel, A. "Petascale Algorithms for Reactor Hydrodynamics," in *J. Phys. Conf. Series*, (2008)
6. Nield, Donald A. and Bejan, Adrian, *Convection in Porous Media 4th ed*. New York,: Springer, 2013.

Nuclear Science and Engineering Division
Argonne National Laboratory
9700 South Cass Avenue, Bldg. 208
Argonne, IL 60439

www.anl.gov